The Astrophysical Journal Letters, 946:L45 (7pp), 2023 April 1 https://doi.org/10.3847/2041-8213/acc58d

Accurate Dust Temperature and Star Formation Rate in the Most Luminous $z > 6$ Quasar in the Hyperluminous Quasars at the Epoch of Reionization (HYPERION) Sample

Roberta Tripodi[1,2,3], Chiara Feruglio[2,3], Francisca Kemper[4,5,6], Francesca Civano[7], Tiago Costa[8], Martin Elvis[7], Manuela Bischetti[1,2], Stefano Carniani[9], Fabio Di Mascia[9], Valentina D'Odorico[2,3,9], Fabrizio Fiore[2,3], Simona Gallerani[9], Michele Ginolfi[10,11], Roberto Maiolino[12,13,14], Enrico Piconcelli[15], Rosa Valiante[15], and Luca Zappacosta[15]

[1] Dipartimento di Fisica, Università di Trieste, Sezione di Astronomia, Via G.B. Tiepolo 11, I-34143 Trieste, Italy; roberta.tripodi@inaf.it
[2] INAF—Osservatorio Astronomico di Trieste, Via G. Tiepolo 11, I-34143 Trieste, Italy
[3] IFPU—Institute for Fundamental Physics of the Universe, via Beirut 2, I-34151 Trieste, Italy
[4] Institute of Space Science (ICE), CSIC, Can Magrans, E-08193 Cerdanyola del Vallès, Barcelona, Spain
[5] ICREA, Pg. Lluís Companys 23, E-08010 Barcelona, Spain
[6] Institut d'Estudis Espacials de Catalunya (IEEC), E-08034 Barcelona, Spain
[7] Center for Astrophysics — Harvard & Smithsonian, Cambridge, MA 02138, USA
[8] Max-Planck-Institut für Astrophysik, Karl-Schwarzschild-Straße 1, D-85748 Garching b. München, Germany
[9] Scuola Normale Superiore, Piazza dei Cavalieri 7 I-56126, Pisa, Italy
[10] Dipartimento di Fisica e Astronomia, Università di Firenze, Via G. Sansone 1, I-50019, Sesto Fiorentino (Florence), Italy
[11] INAF—Osservatorio di Arcetri, Largo E. Fermi 5, I-50125, Florence, Italy
[12] Institute of Astronomy, University of Cambridge, Madingley Road, Cambridge CB3 0HA, UK
[13] Kavli Institute for Cosmology, University of Cambridge, Madingley Road, Cambridge CB3 0HA, UK
[14] Department of Physics and Astronomy, University College London, Gower Street, London WC1E 6BT, UK
[15] INAF—Osservatorio Astronomico di Roma, Via Frascati 33, I-00040 Monte Porzio Catone, Italy
Received 2023 February 7; revised 2023 March 13; accepted 2023 March 20; published 2023 April 5

Abstract

We present ALMA Band 9 continuum observation of the ultraluminous quasi-stellar object (QSO) SDSS J0100 +2802 providing a $\sim 10\sigma$ detection at ~670 GHz. SDSS J0100+2802 is the brightest QSO with the most massive supermassive black hole (SMBH) known at $z > 6$, and we study its dust spectral energy distribution in order to determine the dust properties and the star formation rate (SFR) of its host galaxy. We obtain the most accurate estimate so far of the temperature, mass, and emissivity index of the dust, which are $T_{\rm dust} = 48.4 \pm 2.3$ K, $M_{\rm dust} = (2.29 \pm 0.83) \times 10^7\, M_\odot$, and $\beta = 2.63 \pm 0.23$, respectively. This allows us to measure the SFR with the smallest statistical error for this QSO, SFR $= 265 \pm 32\, M_\odot {\rm yr}^{-1}$. Our results enable us to evaluate the relative growth of the SMBH and host galaxy of J0100+2802. We find that the SMBH is dominating the process of black-hole galaxy growth in this QSO at $z = 6.327$, when the universe was 865 Myr old. Such unprecedented constraints on the host-galaxy SFR and dust temperature can only be obtained through high-frequency observations and highlight the importance of ALMA Band 9 to obtain a robust overview of the buildup of the first quasars' host galaxies at $z > 6$.

Unified Astronomy Thesaurus concepts: Interferometers (805); AGN host galaxies (2017); Quasars (1319); Supermassive black holes (1663)

1. Introduction

In the past decade, the Atacama Large Millimeter/submillimeter Array (ALMA), along with the Northern Extended Millimeter Array, the Very Large Array, and Herschel, have probed the cold gas and dust of quasi-stellar object (QSO) host galaxies. The dust continuum was detected in many $z \sim 6$ QSOs, with far-infrared (FIR) luminosities of $L_{\rm FIR} = 10^{11-13}\, L_\odot$ and dust masses of about $M_{\rm dust} = 10^{7-9}\, M_\odot$ (Decarli et al. 2018; Carniani et al. 2019; Shao et al. 2019). The rest-frame FIR continuum emission originates from dust heated by the ultraviolet (UV) radiation from young and massive stars (Decarli et al. 2018; Venemans et al. 2020; Neeleman et al. 2021) and the active galactic nucleus (AGN) radiation (Schneider et al. 2015; Di Mascia et al. 2021; Walter et al. 2022). The latter contribution is usually neglected when modeling the FIR spectral energy distribution (SED) of $z \sim 6$ QSOs although the AGN heating can contribute 30%–70% of the FIR luminosity (Schneider et al. 2015; Duras et al. 2017). Moreover, dust masses are often determined with huge uncertainties relying only on single-frequency continuum detections. However, if multifrequency ALMA observations are available in the rest-frame FIR, probing both the peak and the Rayleigh–Jeans tail of the dust SED, the dust temperature and mass can be constrained with statistical uncertainties <10%–20% (e.g., Carniani et al. 2019; Tripodi et al. 2022), resulting high accuracy in the determination of the star formation rate (SFR).

In this Letter, we present ALMA Band 9 observations of the QSO SDSS J010013.02+280225.8 (hereafter J0100+28) at $z_{\rm [CII]} = 6.327$ (Wang et al. 2019). Wu et al. (2015) estimated a bolometric luminosity of $L_{\rm bol} = 4.29 \times 10^{14}\, L_\odot$ and a black hole (BH) mass of $M_{\rm BH} = 1.24 \times 10^{10}\, M_\odot$ for J0100+28, making it the most optically luminous QSO with the most massive SMBH known at $z > 6$. Both measurements have been recently confirmed by JWST (Eilers et al. 2022). Wang et al. (2019) performed a multifrequency analysis of the dust SED,

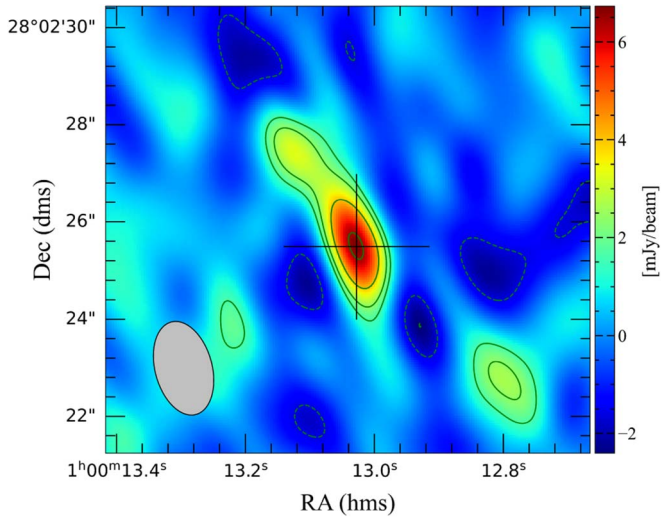

Figure 1. 670.9 GHz dust continuum map of QSO J0100+28 (levels -3σ, -2σ, 2σ, 3σ, 5σ, and 8σ, $\sigma = 0.8$ mJy beam^{-1}). The clean beam ($1.97'' \times 1.17''$) is indicated in the lower left corner of the diagram. The cross indicates the position of the continuum peak.

but they could not obtain a precise determination of the dust properties, concluding that J0100+28 has either high dust emissivity ($\beta \gtrsim 2$) or high dust temperature ($T_{\rm dust} \gtrsim 60$ K) or a combination of thereof.

J0100+28 belongs to the HYPerluminous quasars at the Epoch of ReionizatION (HYPERION) sample of $z > 6$ QSOs, selected to include the QSOs with the most massive SMBH at their epoch, possibly resulting from an exceptionally fast mass growth during their accretion history. The sample consists of 17 QSOs with $L_{\rm bol} = 10^{47.3}$ erg s^{-1}, SMBH masses in the range $M_{\rm BH} = 10^{9}$–$10^{10}\,M_{\odot}$, and Eddington ratios >0.3–0.4. The HYPERION sample and the details of its selection will be presented in L. Zappacosta et al. 2023 (in preparation).

The goal of this work is to derive the most accurate estimate of the dust mass, dust temperature, and therefore of the SFR for the host galaxy of J0100+28. We adopt a ΛCDM cosmology from Planck Collaboration et al. (2020): $H_0 = 67.4$ km s^{-1} Mpc^{-1}, $\Omega_m = 0.315$, and $\Omega_\Lambda = 0.685$. Thus, the angular scale is 5.66 kpc arcsec^{-1} at $z = 6.3$.

2. Observation

We analyze the data set 2021.2.00151.S from the ALMA 7 m array, designed to detect the continuum emission at a frequency of 670.91 GHz in Band 9, and with a total integration time of 2.2 hr. The visibility calibration and imaging are performed through the Common Astronomy Software Applications (CASA; McMullin et al. 2007), version 5.1.1–5. We apply `tclean` using natural weighting and a 3σcleaning threshold. We image the continuum by collapsing all channels, selected by inspecting the visibilities in all spectral windows. We obtain a clean beam of ($1.97'' \times 1.17''$), corresponding to a spatial resolution of ∼11 kpc, and an rms noise of 0.8 mJy beam^{-1} in the continuum.

3. Analysis

3.1. QSO Continuum Emission and Dust Properties

Figure 1 presents the 670.9 GHz continuum emission map of J0100+28. The peak flux density is 6.99 ± 0.71 mJy beam^{-1}. The source is not spatially resolved. We check that the other FIR and radio flux measurements were extracted from a region similar to our resolution.[16]

We perform an SED fitting using the continuum emission measured at ∼671 GHz, together with the emissions presented in Wang et al. (2019) from 32 to 353 GHz, and in Liu et al. (2022) at 1.5, 6, and 10 GHz. Although we are interested in the cold dust properties of the QSO host galaxy, such as $T_{\rm dust}$, $M_{\rm dust}$ and β, we consider also the contribution of the lower frequency emission to the dust SED since in general it may not be negligible. Liu et al. (2022) noticed a time variability among their and previous measurements of the radio continuum in the range [6–10] GHz. For the sake of simplicity, we consider the most recent measurements of the radio continuum emission (i.e., those from Liu et al. 2022). However, we verified that our results do not change by considering all the measurements available in the radio band.

We model the dust continuum with a modified blackbody (MBB) function and the low-frequency radio emission using a power law with an exponential cutoff (PLCO). Details about the fitting functions and procedure can be found in the Appendix. The model has six fitting parameters: dust temperature ($T_{\rm dust}$), dust mass ($M_{\rm dust}$), dust emissivity index (β) entering in the MBB function, the normalization (n), the radio power-law spectral index (α), and the cutoff frequency ($\nu_{\rm cutoff}$) for the PLCO. It is worth to stress that the galaxy is likely characterized by a distribution of dust temperatures, which may reach hundreds of kelvin close to the AGN (see, e.g., Walter et al. 2022) and may decrease toward the outskirts; hence, the temperature derived from the SED fitting should be interpreted as an "effective" dust temperature.[17] The best-fit model has $T_{\rm dust} = 48.4 \pm 2.3$ K, $M_{\rm dust} = (2.29 \pm 0.83) \times 10^{7}\,M_{\odot}$, $\beta = 2.63 \pm 0.23$, $n = 0.08 \pm 0.01$ mJy, $\alpha = 0.48 \pm 0.09$, and $\nu_{\rm cutoff} = 235 \pm 100$ GHz. Figure 2 shows the observed SED fitted by our best-fit model (left panel) and the posterior distributions for the dust parameters (right panel). Posterior distributions of all parameters are reported in the Appendix. We find a gas-to-dust ratio (GDR) $= 236 \pm 155$ based on our $M_{\rm dust}$ estimate and the molecular gas mass obtained by Wang et al. (2019; see Table 1). This is in agreement with GDRs found in ultraluminous QSOs at $z \sim 2$–4 (Bischetti et al. 2021) and in local galaxies at solar metallicities (De Vis et al. 2019). This latter comparison would imply that J0100+28's host galaxy has already been highly enriched with metals.

We estimate the total infrared (TIR) luminosity for the best-fit model by integrating from 8 to 1000 μm rest frame, obtaining $L_{\rm TIR} = 5.30 \pm 0.64 \times 10^{12}\,L_{\odot}$. This would imply an SFR of $530 \pm 64\,M_{\odot}$ yr^{-1}, adopting a Chabrier initial mass function (Chabrier 2003). However, several observations and radiative transfer simulations suggested that the radiative output of luminous QSOs substantially contributes to dust heating on a kiloparsec scale (Schneider et al. 2015; Di Mascia et al. 2021; Walter et al. 2022). Duras et al. (2017) showed that on average, ∼50% of the total IR luminosity in QSOs with $L_{\rm bol} > 10^{47}$ erg s^{-1} is due to dust heated by the AGN radiation. Recently, Di Mascia et al. (2023) found a correction factor of one-thirtieth for the SFR of the brightest object in their sample.

[16] Wang et al. (2019) used tapered maps at 1.5″ in order not to miss the fainter extended emission. Liu et al. (2022) also tapered their 6 and 10 GHz maps, which had a resolution of ∼1.5″, to match the resolution of the 1.5 GHz map (∼4″), and they do not find significant differences in flux density between the tapered and the full-resolution maps.

[17] We adopt the term "effective temperature" since we are not able to map the spatial distribution of the dust temperatures across the galaxy, similarly to the definition of the effective temperature of a star.

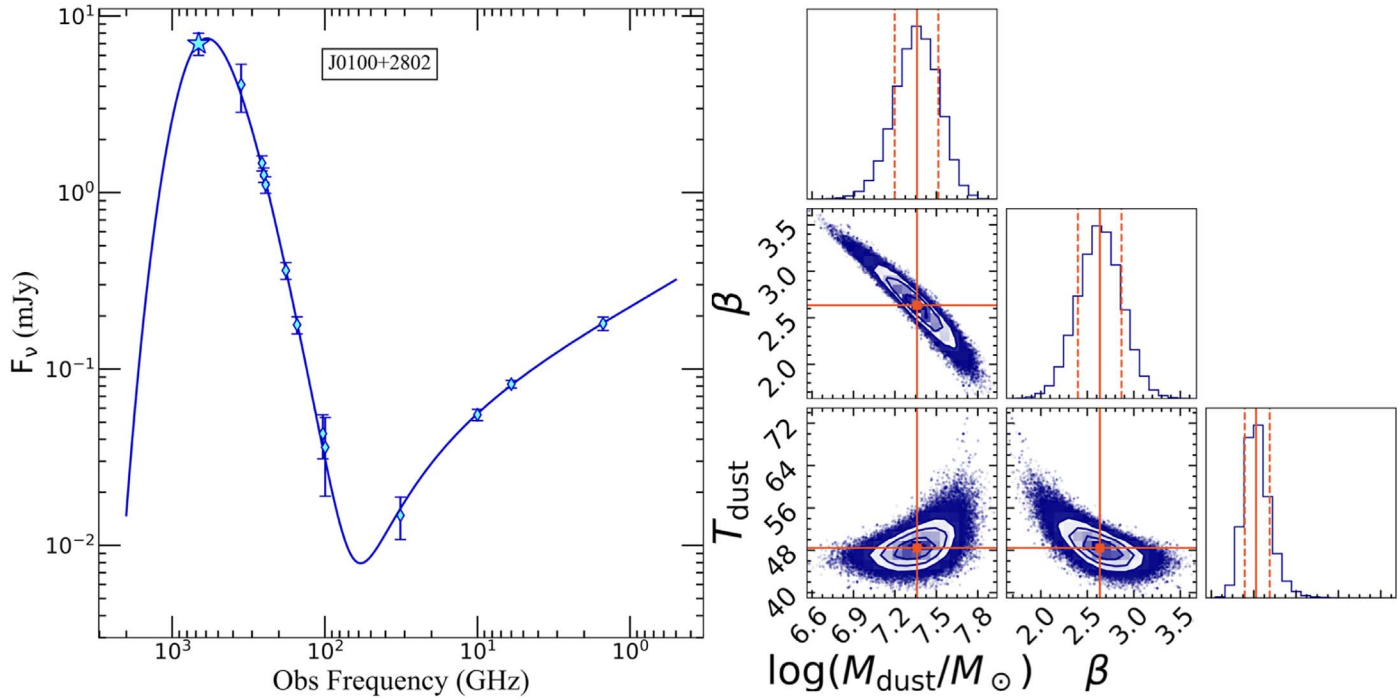

Figure 2. Left panel: SED of J0100+28 using our new ALMA 670.91 GHz data (cyan star); the continuum fluxes from 32 to 353 GHz (Wang et al. 2019) and at 1.5, 6, and 10 GHz (Li et al. 2022; cyan diamonds). The best-fitting curve is shown as a blue solid line. Right panel: corner plot showing the posterior probability distributions of T_{dust}, M_{dust}, and β. Orange solid lines indicate the best-fitting value for each parameter, while the dashed lines mark the 16th and 84th percentiles for each parameter.

Table 1
Properties of SDSS J0100+2802

T_{dust}	[K]	48.4 ± 2.3
M_{dust}	[$10^7\,M_\odot$]	2.29 ± 0.83
β		2.63 ± 0.23
SFR[a]	[$M_\odot\,yr^{-1}$]	265 ± 32
GDR		236 ± 155
M_{gas}[b]	[$10^{10}\,M_\odot$]	0.54 ± 0.16
M_{dyn}(CV)[c]	[$10^{10}\,M_\odot$]	$\sim$890
M_{dyn}(VT)[d]	[$10^{10}\,M_\odot$]	3.25 ± 0.46
M_{BH}[e]	[$10^{10}\,M_\odot$]	1.05

Notes. Quantities above the line are from this work, while the others are taken from Wang et al. (2019).
[a] The SFR is corrected by a factor of 50%, accounting for the contribution of the QSO.
[b] The gas mass is estimated within a diameter of $\sim$1.4 kpc (Wang et al. 2019).
[c] Dynamical mass estimated using the circular velocity, assuming a disk inclination of 5° within 1.8 kpc radius (Wang et al. 2019).
[d] Dynamical mass estimated using the virial theorem within 1.8 kpc radius (Wang et al. 2019).
[e] BH mass from Mg II emission line (C. Mazzucchelli et al. 2023, in preparation).

However, the L_{bol} of J0100 is above the range explored in their simulations, and moreover, J0100 has very peculiar properties in terms of UV magnitude and dust temperatures with respect to the simulated QSOs in Di Mascia et al. (2023). Therefore, we consider the average correction proposed by Duras et al. (2017) as the most appropriate choice, and we obtain SFR $= 265 \pm 32\,M_\odot yr^{-1}$.

4. Discussion and Conclusions

By fitting the dust SED of the QSO J0100+28, we found that our observation in Band 9 favors a dust temperature lower than the effective dust temperatures found in simulations in bright ($L_{bol} > 10^{13}\,L_\odot$) quasar hosts ($\sim$90 K, e.g., Di Mascia et al. 2023). This discrepancy can be due to different dust spatial distributions between the simulated objects and J0100+28 or to limits in the dust modeling and radiative transfer postprocessing (e.g., the absence of a dusty torus in Di Mascia et al. 2021). With the current unresolved observation we are able neither to constrain different temperature components nor to determine the temperature distribution across the galaxy. The value found for the emissivity index is higher than $\beta = 1.6$ found for the average SED of high-z QSOs (Beelen et al. 2006). However, as noted by Beelen et al. (2006), large variations of β are found when considering individual QSO SED. Only excluding the Band 9 data, we would obtain a good fit with $\beta < 2$, having then a factor of 2 higher temperature (see also Wang et al. 2019). This shows that the results can be misguided by relying only on the lowest frequency data points, while Band 9 is essential to reliably estimate dust parameters up to the highest redshifts. Indeed, Novak et al. (2019), using observations up to Band 8 at $\sim$404 GHz, could not constrain T_{dust} in the $z = 7.54$ quasar ULAS J1342+0928. This work provides the first measurement of the Band 9 continuum of a luminous QSO host galaxy. Similarly, Bakx et al. (2021) used Band 9 observations to constrain T_{dust} for a galaxy at $z = 7.13$.

It is not straightforward to assess the physical reasons of the high β value. In principle, β depends on the physical properties and chemical composition of the grains and possibly on environment and temperature. There are cases in which β can

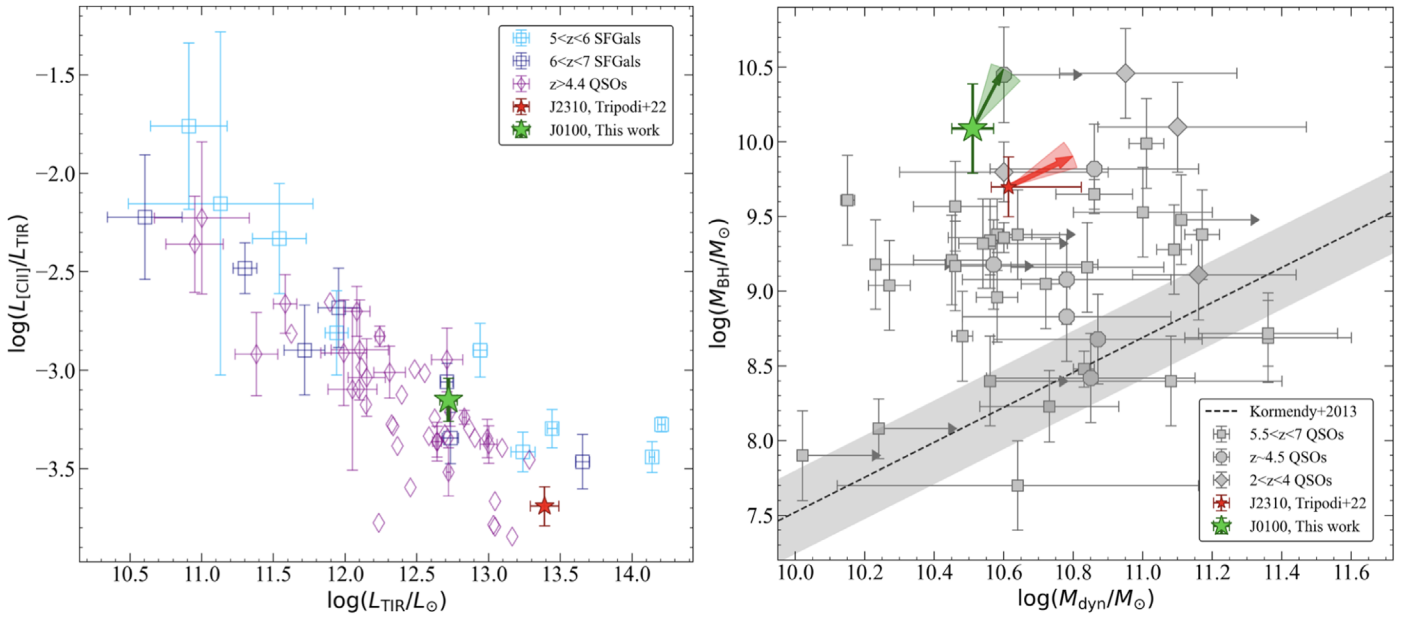

Figure 3. Left panel: [C II]-to-TIR luminosity ratio vs. TIR luminosity. We show our result for QSO J0100+28 (green star) compared with QSO J2310+18 at $z = 6.0028$ (red star); two samples of star-forming galaxies at $5 < z < 6$ and $6 < z < 7$ (cyan and blue squares, respectively, taken from Lagache et al. 2018); and a sample of QSOs at $z > 4.4$ (violet diamonds, from Bischetti et al. 2021 and Decarli et al. 2018). Right panel: BH mass vs. dynamical mass for J0100+28 (green star), compared with QSO J2310+18 at $z = 6.0028$ (red star, Tripodi et al. 2022), WISSH QSOs at $z \sim 2$–4 (gray diamonds, Bischetti et al. 2021), and luminous $z \sim 4$–7 QSOs (gray circles and gray squares, Mortlock et al. 2011; Willott et al. 2013; De Rosa et al. 2014; Kashikawa et al. 2015; Kimball et al. 2015; Willott et al. 2015; Venemans et al. 2016; Trakhtenbrot et al. 2017; Venemans et al. 2017; Willott et al. 2017; Feruglio et al. 2018; Neeleman et al. 2021). Black dashed line (and shaded area) is the local relation from Kormendy & Ho (2013). For J0100+28 (J2310+18), the slope of the arrow, with its uncertainty, indicates how much the growth efficiency of the SMBH is increasing (slowing down) with respect to the growth of the host galaxy.

be larger than two (see, e.g., Valiante et al. 2011; Galliano et al. 2018). Spatially resolved studies in low-z galaxies showed a spread of β within a single galaxy, probably due to the temperature mixing or the different properties of the grain populations or both. The strong anticorrelation between $T_{\rm dust}$ and β can arise from the Markov Chain Monte Carlo (MCMC) fitting procedure itself, mainly if there is a massive amount of cold dust (i.e., $T \lesssim 10$ K; Galliano et al. 2018). However, in our case, the accurate sampling of the SED from low to high frequency significantly relaxed the strength of $T_{\rm dust} - \beta$ anticorrelation (Figure 2). Therefore, we are confident that the estimates of β and $T_{\rm dust}$ are not strongly biased due to the effect of this anticorrelation. Finding a physical explanation for the high value of β would require studies of the properties of the dust grains and/or a detailed analysis of the temperature mixing and is beyond the scope of this Letter.

The left panel of Figure 3 shows the ratio of integrated [C II] to TIR luminosity for J0100+28 and a compilation of high-redshift QSOs and galaxies (see caption). For J0100+28 we find $L_{\rm [CII]}/L_{\rm TIR} \sim 7 \times 10^{-4}$, given $L_{\rm [CII]} = 3.7 \times 10^9\, L_\odot$ (Wang et al. 2019). This [C II] deficit is also predicted for high-z galaxies by semi-analytical models of galaxy evolution (e.g., Lagache et al. 2018), where the [C II] deficit arises from the high intensity of the interstellar radiation field. Our estimate of $L_{\rm [CII]}/L_{\rm TIR}$ agrees well with their results at $z \sim 6$ when we extrapolate their predictions at higher $L_{\rm TIR}$. Carniani et al. (2018) found that the local $L_{\rm [CII]}$−SFR relation for star-forming galaxies (see De Looze et al. 2014) is still valid at high-z but with a dispersion twice higher than observed locally. Our results agree within $<1\sigma$ with the correlation of Carniani et al. (2018) and with the results for high-z galaxies of Lagache et al. (2018).

We evaluate the evolutionary state of the SMBH—host galaxy system. Wang et al. (2019) provide two estimates for $M_{\rm dyn}$, one based on the assumption that the [C II] line arises from a rotating disk with very low inclination and the other using the virial theorem with the hypothesis that the gas is supported by random motion (see Table 1). Although both estimates carry large uncertainties, the latter is in agreement with the dynamical masses commonly measured for other QSOs at high-z (see right panel of Figure 3), and we adopt it as a lower limit. The molecular gas mass is $M_{\rm gas} = 5.4 \times 10^9\, M_\odot$, and this implies a molecular gas fraction $\mu = M_{\rm gas}/M_* = M_{\rm gas}/(M_{\rm dyn} - M_{\rm BH} - M_{\rm gas}) = 0.4$, which is remarkably lower than the typical gas fractions at $z \sim 3$–4 (Tacconi et al. 2018). We define the growth efficiency of the galaxy as $\mathrm{SFR}/M_{\rm g+s}$, where $M_{\rm g+s} = M_{\rm gas} + M_*$, and the SFR is corrected for the QSO contribution. We use $M_{\rm g+s}$, instead of $M_{\rm dyn}$ (as in Tripodi et al. 2022), since the BH mass is not negligible ($M_{\rm BH} \sim 40\% M_{\rm dyn}$; Wang et al. 2019) and can bias our results.[18] We obtain $M_{\rm g+s} = 2.01 \times 10^{10}\, M_\odot$; therefore, $\mathrm{SFR}/M_{\rm g+s} = 1.3 \times 10^{-8}\,\mathrm{yr}^{-1}$. On the other hand, we derive a BH growth efficiency,[19] $(1-\epsilon)\dot{M}_{\rm BH}/M_{\rm BH} = 2.5 \times 10^{-8}\,\mathrm{yr}^{-1}$, where we use the BH mass derived from Mg II (Table 1) and assume a radiative efficiency $\epsilon = 0.1$ (e.g., Marconi et al. 2004). The right panel of Figure 3 shows $M_{\rm BH}$ versus $M_{\rm dyn}$ for J0100+28, J2310+18 (Tripodi et al. 2022) and a compilation of QSOs at different redshifts, comparing them with the local $M_{\rm BH} - M_{\rm dyn}$ relation. The majority of QSOs, including J0100+28, lie above the local relation in the BH

[18] To be consistent, we recompute the growth efficiency of the galaxy for J2310 using $M_{\rm g+s}$, and we changed the slope of the arrow with respect to the one shown in Tripodi et al. (2022). However, the results do not change significantly since $M_{\rm g+s} \simeq M_{\rm dyn}$ for J2310.

[19] $\dot{M}_{\rm BH} = L_{\rm bol}/(\epsilon\, c^2)$, where ϵ is the radiative efficiency, and c is the speed of light.

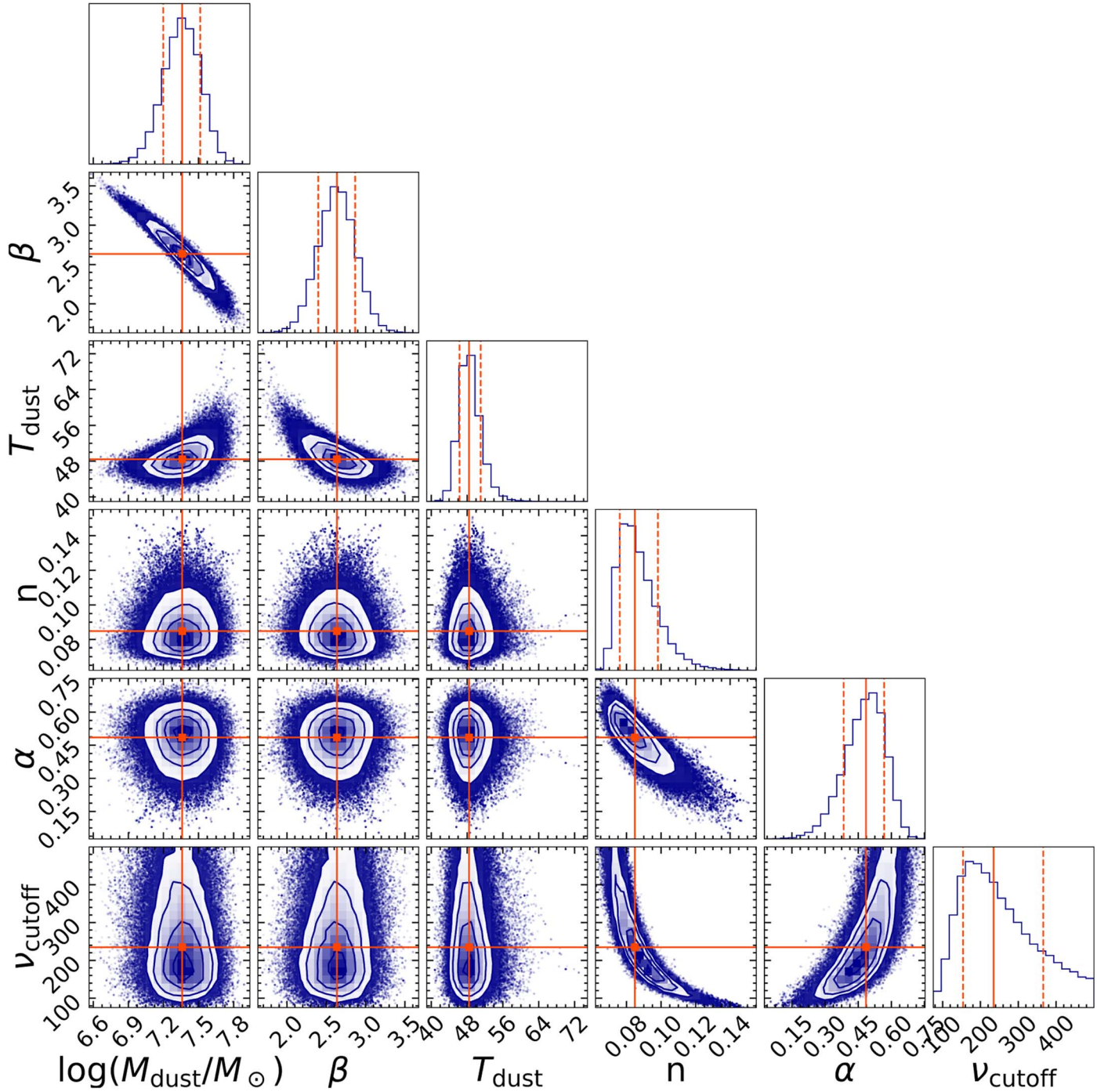

Figure 4. Corner plot showing the six-dimensional posterior probability distributions of $T_{\rm dust}$, $M_{\rm dust}$, β, n, α, and $\nu_{\rm cutoff}$. Orange solid lines on the posterior probability distributions indicate the best-fitting value for each parameter, while the dashed lines mark the 16th and 84th percentiles for each parameter.

dominance regime (Volonteri 2012). However, this tension can be partially softened if accounting for the uncertainties on the dynamical mass estimates. These mainly depend on the determination of the disk inclination and can be significantly high for some QSOs (Valiante et al. 2014; Pensabene et al. 2020). This is also the case of J0100+28, whose $M_{\rm dyn}$ can be, in principle, as high as $10^{12}\,M_{\odot}$ (see Table 1). For J0100+28, we found $(1-\epsilon)\dot{M}_{\rm BH}/M_{\rm BH} > {\rm SFR}/M_{\rm g+s}$, suggesting that the BH is still dominating the process of a BH galaxy growing in this QSO at $z = 6.327$. This result is still valid if considering lower SFR (adopting the correction by Di Mascia et al. 2023) and/or higher $M_{\rm dyn}$ (i.e., higher $M_{\rm g+s}$ at fixed BH mass) since the galaxy growth factor would be even smaller. Our results do not consider the gas inflow. However, we expect this term to contribute on average to both SFR and $M_{\rm g+s}$, leaving their ratio mostly unaffected. On the other hand, in QSO J2310+18 at $z \sim 6$, AGN feedback might be slowing down the accretion onto the SMBH, while the host galaxy grows fast (Bischetti et al. 2022; Tripodi et al. 2022). The different evolutionary states of J0100+28 and J2310+18, separated by only ∼60 Myr (i.e., $\Delta z \sim 0.3$), arise mainly from the difference in their BH masses (i.e., $M_{\rm BH,J0100+28} \sim 2 \times M_{\rm BH,J2310+18}$) and in the SFRs (i.e., ${\rm SFR}_{J0100+28} \sim 0.2 \times {\rm SFR}_{J2310+18}$). In principle, ${\rm SFR}/M_{*}$ is a better probe of the galaxy growth; however, this is not available

for most high-redshift QSOs. For J0100+28, using SFR/M_* would not affect our results since $M_{g+s} \approx M_*$. For J2310, $M_* \ll M_{g+s}$, therefore resulting in an even flatter slope. The BH-dominated growth of J0100+28 matches the qualitative expectations for the evolutionary state of the HYPERION QSOs that were selected to be the most luminous QSOs with the most massive SMBH at their epochs.

We compare our results with "zoom-in" simulations of QSOs using the moving-mesh code AREPO, following BH growth and feedback via energy-driven outflows (Costa et al. 2014, 2015). We found that simulations reproduce BHs only up to masses $\sim 10^9\,M_\odot$ that have host galaxies with dynamical masses $\sim 10^{11}\,M_\odot$. These are considerably more massive than the J0100+28 host galaxy. The growth of the system is characterized by intermittent phases, where the BH and galaxy-dominated growth phases change on short timescales. Hence, the diagnostic power of the relation $(1-\epsilon)\dot{M}_{BH}/M_{BH}$ - SFR/M_{g+s} needs to be validated in larger samples that we plan to investigate in a forthcoming work.

In summary, this work allowed us to measure the SFR with the smallest statistical error, reaching an accuracy of ∼15% for QSO J0100+28. Such unprecedented constraints on the host-galaxy SFR (and T_{dust}) highlight the critical role of ALMA Band 9 to obtain a robust overview of the buildup of SMBHs and their massive host galaxies at the Epoch of Reionization. The systematic uncertainty on the SFR is still high due to the uncertainty in the estimate of the QSO contribution. Recently, Tsukui et al. (2023) estimated this contribution for a $z = 4.4$ QSO using high-resolution ALMA observations up to band 9. Given our current unresolved observation, we are not able to use the same approach. However, we plan to determine this correction factor in forthcoming works using both high-resolution observations and radiative transfer models to reproduce the observed SED.

We thank the anonymous referee for the useful suggestions that helped us improving this work. This paper makes use of the following ALMA data: ADS/JAO.ALMA#2021.2.00151. S. ALMA is a partnership of ESO (representing its member states), NFS (USA) and NINS (Japan), together with NRC (Canada), MOST and ASIAA (Taiwan) and KASI (Republic of Korea), in cooperation with the Republic of Chile. The Joint ALMA Observatory is operated by ESO, AUI/NRAO and NAOJ. R.T. acknowledges financial support from the University of Trieste. R.T., C.F., F.F., and M.B. acknowledge support from PRIN MIUR project "black hole winds and the Baryon Life Cycle of Galaxies: the stone-guest at the galaxy evolution supper," contract #2017PH3WAT. R.T. and M.B. acknowledge support from INAF grant 1.05.12.04.01 "Mini-feedback". F.K. acknowledges the Spanish program Unidad de Excelencia María de Maeztu CEX2020-001058-M, financed by MCIN/AEI/10.13039/501100011033. S.C. is supported by the European Union (ERC, WINGS,101040227). R.M. acknowledges ERC Advanced Grant 695671 QUENCH, and support from the UK Science and Technology Facilities Council (STFC). R.M. also acknowledges funding from a research professorship from the Royal Society. L.Z. acknowledges financial support from the Bando Ricerca Fondamentale INAF 2022 Large Grant "Toward an holistic view of the Titans: multi-band observations of z > 6 QSOs powered by greedy supermassive black-holes" and from INAF "Progetti di Ricerca di Rilevante Interesse Nazionale" (PRIN), Bando 2019 "Piercing through the clouds: a multiwavelength study of obscured accretion in nearby supermassive black holes". F.C. is supported by funding of the NASA Physics of the Cosmos Program.

Facility: ALMA.

Software: astropy, CASA (v5.1.1-5, McMullin et al. 2007).

Appendix
Posterior Distributions

We model the dust continuum with an MBB function given by

$$S^{obs}_{\nu_{obs}} = S^{obs}_{\nu/(1+z)} = \frac{\Omega}{(1+z)^3}[B_\nu(T_{dust}(z)) - B_\nu(T_{CMB}(z))](1-e^{-\tau_\nu}), \quad \text{(A1)}$$

where $\Omega = (1+z)^4 A_{gal} D_L^{-2}$ is the solid angle with A_{gal} and D_L is the surface area and luminosity distance of the galaxy, respectively (Carniani et al. 2019). The dust optical depth is

$$\tau_\nu = \frac{M_{dust}}{A_{galaxy}} k_0 \left(\frac{\nu}{250\ \text{GHz}}\right)^\beta, \quad \text{(A2)}$$

with β the emissivity index and $k_0 = 0.45\ \text{cm}^2\ \text{g}^{-1}$ the mass absorption coefficient (Beelen et al. 2006). The solid angle is estimated using the continuum mean size from resolved observations (Wang et al. 2019). The effect of the cosmic microwave background (CMB) on the dust temperature is given by

$$T_{dust}(z) = ((T_{dust})^{4+\beta} + T_0^{4+\beta}[(1+z)^{4+\beta} - 1])^{\frac{1}{4+\beta}}, \quad \text{(A3)}$$

with $T_0 = 2.73$ K. We also considered the contribution of the CMB emission given by $B_\nu(T_{CMB}(z) = T_0(1+z))$ (da Cunha et al. 2013).

We model the low-frequency radio emission using a PLCO that is

$$F_{\nu_{rest}} = n \times (\nu_{rest}/\nu_0)^{-\alpha} \times \exp(-\nu_{rest}/\nu_{cutoff}), \quad \text{(A4)}$$

where n is the normalization; α is the radio power-law spectral index; and ν_0 and ν_{cutoff} are the reference frequency and the cutoff frequency, respectively. We set $\nu_0 = 59$ GHz to ease the fitting procedure and in order to minimize the covariance between n and α. This choice does not affect our results.

The total model has six fitting parameters: dust temperature (T_{dust}), dust mass (M_{dust}), β entering in the MBB function, and n, α, and ν_{cutoff} for the PLCO. We explore the six-dimensional parameter space using an MCMC algorithm implemented in the `EMCEE` package (Foreman-Mackey et al. 2013). We assume uniform priors for the fitting parameters: $10\ \text{K} < T_{dust} < 300$ K, $10^5\,M_\odot < M_{dust} < 10^9\,M_\odot$, $1.0 < \beta < 3.0$, $0.001\ \text{mJy} < n < 0.5$ mJy, $0.01 < \alpha < 1.0$, and $75.0\ \text{GHz} < \nu_{cutoff} < 500\ \text{GHz}$. The best-fit model has $T_{dust} = 48.4 \pm 2.3$ K, $M_{dust} = (2.29 \pm 0.83) \times 10^7\,M_\odot$, $\beta = 2.63 \pm 0.23$, $n = 0.08 \pm 0.01$ mJy, $\alpha = 0.48 \pm 0.09$, and $\nu_{cutoff} = 235 \pm 100$ GHz obtained from an MCMC with 60 chains, 6000 trials, and a burn-in phase of ∼100. Figure 4 shows the posterior distributions of the six fitting parameters T_{dust}, M_{dust}, β, n, α, and ν_{cutoff}.

ORCID iDs

Roberta Tripodi https://orcid.org/0000-0002-9909-3491
Chiara Feruglio https://orcid.org/0000-0002-4227-6035

Francisca Kemper https://orcid.org/0000-0003-2743-8240
Francesca Civano https://orcid.org/0000-0002-2115-1137
Tiago Costa https://orcid.org/0000-0002-6748-2900
Martin Elvis https://orcid.org/0000-0001-5060-1398
Manuela Bischetti https://orcid.org/0000-0002-4314-021X
Stefano Carniani https://orcid.org/0000-0002-6719-380X
Valentina D'Odorico https://orcid.org/0000-0003-3693-3091
Fabrizio Fiore https://orcid.org/0000-0002-4031-4157
Simona Gallerani https://orcid.org/0000-0002-7200-8293
Michele Ginolfi https://orcid.org/0000-0002-9122-1700
Roberto Maiolino https://orcid.org/0000-0002-4985-3819
Enrico Piconcelli https://orcid.org/0000-0001-9095-2782
Rosa Valiante https://orcid.org/0000-0003-3050-1765
Luca Zappacosta https://orcid.org/0000-0002-4205-6884

References

Bakx, T. J. L. C., Sommovigo, L., Carniani, S., et al. 2021, MNRAS, 508, L58
Beelen, A., Cox, P., Benford, D. J., et al. 2006, ApJ, 642, 694
Bischetti, M., Feruglio, C., D'Odorico, V., et al. 2022, Natur, 605, 244
Bischetti, M., Feruglio, C., Piconcelli, E., et al. 2021, A&A, 645, A33
Carniani, S., Gallerani, S., Vallini, L., et al. 2019, MNRAS, 489, 3939
Carniani, S., Maiolino, R., Amorin, R., et al. 2018, MNRAS, 478, 1170
Chabrier, G. 2003, PASP, 115, 763
Costa, T., Sijacki, D., & Haehnelt, M. G. 2015, MNRAS, 448, L30
Costa, T., Sijacki, D., Trenti, M., & Haehnelt, M. G. 2014, MNRAS, 439, 2146
da Cunha, E., Groves, B., Walter, F., et al. 2013, ApJ, 766, 13
De Looze, I., Cormier, D., Lebouteiller, V., et al. 2014, A&A, 568, A62
De Rosa, G., Venemans, B. P., Decarli, R., et al. 2014, ApJ, 790, 145
De Vis, P., Jones, A., Viaene, S., et al. 2019, A&A, 623, A5
Decarli, R., Walter, F., Venemans, B. P., et al. 2018, ApJ, 854, 97
Di Mascia, F., Carniani, S., Gallerani, S., et al. 2023, MNRAS, 518, 3667
Di Mascia, F., Gallerani, S., Behrens, C., et al. 2021, MNRAS, 503, 2349
Duras, F., Bongiorno, A., Piconcelli, E., et al. 2017, A&A, 604, A67
Eilers, A.-C., Simcoe, R. A., Yue, M., et al. 2022, arXiv:2211.16261
Feruglio, C., Fiore, F., Carniani, S., et al. 2018, A&A, 619, A39
Foreman-Mackey, D., Hogg, D. W., Lang, D., & Goodman, J. 2013, PASP, 125, 306
Galliano, F., Galametz, M., & Jones, A. P. 2018, ARA&A, 56, 673
Kashikawa, N., Ishizaki, Y., Willott, C. J., et al. 2015, ApJ, 798, 28
Kimball, A. E., Lacy, M., Lonsdale, C. J., & Macquart, J. P. 2015, MNRAS, 452, 88
Kormendy, J., & Ho, L. C. 2013, ARA&A, 51, 511
Lagache, G., Cousin, M., & Chatzikos, M. 2018, A&A, 609, A130
Li, J., Venemans, B. P., Walter, F., et al. 2022, ApJ, 930, 27
Liu, Y., Wang, R., Momjian, E., et al. 2022, ApJ, 929, 69
Marconi, A., Risaliti, G., Gilli, R., et al. 2004, MNRAS, 351, 169
McMullin, J. P., Waters, B., Schiebel, D., Young, W., & Golap, K. 2007, in ASP Conf. Ser. 376, Astronomical Data Analysis Software and Systems XVI 376, ed. R. A. Shaw, F. Hill, & D. J. Bell (San Francisco, CA: ASP), 127
Mortlock, D. J., Warren, S. J., Venemans, B. P., et al. 2011, Natur, 474, 616
Neeleman, M., Novak, M., Venemans, B. P., et al. 2021, ApJ, 911, 141
Novak, M., Bañados, E., Decarli, R., et al. 2019, ApJ, 881, 63
Pensabene, A., Carniani, S., Perna, M., et al. 2020, A&A, 637, A84
Planck Collaboration, Aghanim, N., Akrami, Y., et al. 2020, A&A, 641, A6
Schneider, R., Bianchi, S., Valiante, R., Risaliti, G., & Salvadori, S. 2015, A&A, 579, A60
Shao, Y., Wang, R., Carilli, C. L., et al. 2019, ApJ, 876, 99
Tacconi, L. J., Genzel, R., Saintonge, A., et al. 2018, ApJ, 853, 179
Trakhtenbrot, B., Lira, P., Netzer, H., et al. 2017, ApJ, 836, 8
Tripodi, R., Feruglio, C., Fiore, F., et al. 2022, A&A, 665, A107
Tsukui, T., Wisnioski, E., Krumholz, M. R., & Battisti, A. 2023, arXiv:2302.07272
Valiante, R., Schneider, R., Salvadori, S., & Bianchi, S. 2011, MNRAS, 416, 1916
Valiante, R., Schneider, R., Salvadori, S., & Gallerani, S. 2014, MNRAS, 444, 2442
Venemans, B. P., Walter, F., Decarli, R., et al. 2017, ApJ, 837, 146
Venemans, B. P., Walter, F., Neeleman, M., et al. 2020, ApJ, 904, 130
Venemans, B. P., Walter, F., Zschaechner, L., et al. 2016, ApJ, 816, 37
Volonteri, M. 2012, Sci, 337, 544
Walter, F., Neeleman, M., Decarli, R., et al. 2022, ApJ, 927, 21
Wang, F., Wang, R., Fan, X., et al. 2019, ApJ, 880, 2
Willott, C. J., Bergeron, J., & Omont, A. 2015, ApJ, 801, 123
Willott, C. J., Bergeron, J., & Omont, A. 2017, ApJ, 850, 108
Willott, C. J., Omont, A., & Bergeron, J. 2013, ApJ, 770, 13
Wu, X.-B., Wang, F., Fan, X., et al. 2015, Natur, 518, 512